

A Comparative Analysis of Phase-Domain ADC and Amplitude-Domain IQ ADC

Yao Liu, *Student Member, IEEE*, Reza Lotfi, *Senior Member, IEEE*, Yongchang Hu, *Student Member, IEEE*, and Wouter A. Serdijn, *Fellow, IEEE*

Abstract—A phase-domain analog-to-digital converter (PhADC) is a promising alternative to a pair of amplitude-domain in-phase and quadrature (IQ) ADCs for low power FSK/PSK demodulation, but the fundamental benefits and limitations of the PhADC over the IQ ADC have not been precisely quantified as yet. In this paper, analytical methods are proposed to comprehensively compare the PhADC and the IQ ADC. Phase signal-to-noise ratio (SNR) expressions of the two ADC types are formulated analytically to facilitate a quantitative comparison of them. In comparison with the IQ ADC, the PhADC is a more compact quantization and demodulation solution when interference accommodation is not required. Moreover, considering a flash ADC as an example of the low resolution (3-4 bit) IQ ADC, the PhADC has a lower theoretical energy limit than the flash ADC for a given phase ENOB. IQ offsets and amplitude mismatch impose unique nonlinearities on the PhADC due to the nonlinear amplitude-to-phase conversion. The understanding of this nonlinearity leads to a phase-domain mismatch and offset detection technique. Phase SNR is explicitly related to input noise for both ADCs, and to comparator offsets for the PhADC, respectively. All of the results prove that the PhADC is a promising quantization and demodulation solution.

Index Terms—Amplitude mismatch, in-phase and quadrature (IQ) ADC, offset, phase-domain analog-to-digital converter (PhADC), phase nonlinearity, phase signal-to-noise ratio (SNR).

I. INTRODUCTION

POWER efficient ADCs and demodulators are in high demand for low power wireless receivers. Downconverted in-phase and quadrature (I and Q) signals are commonly quantized by a pair of amplitude analog-to-digital converters (IQ ADC), and are subsequently demodulated in the digital domain. Alternatively, modulation-specific quantization and demodulation approaches can be used by exploiting the unique properties of the modulation schemes at hand. One promising example is a phase-domain ADC (PhADC)-based FSK and PSK demodulator for Bluetooth, Bluetooth low energy (BLE) and ZigBee receivers [1]–[8]. FSK and PSK modulation schemes are widely adopted in low power short-range wireless standards, e.g., BLE, Zigbee, IEEE 802.15.6, etc. The fact that in FSK and PSK modulation schemes data information is encoded in the signal phase alone is utilized by the PhADC by only quantizing phase information as opposed to I and Q amplitude information, resulting in a compact and energy-efficient system architecture.

Manuscript received August 19, 2014; revised October 24, 2014; accepted November 10, 2014. This paper was recommended by Associate Editor S. Cho.

Y. Liu, Y. Hu and W. A. Serdijn are with the Faculty of Electrical Engineering, Mathematics and Computer Science, Delft University of Technology, Delft, 2628CD, The Netherlands (e-mail: y.liu-2@tudelft.nl; y.hu-1@tudelft.nl; serdijn@ieee.org).

R. Lotfi is with the Faculty of Electrical Engineering, Mathematics and Computer Science, Delft University of Technology, Delft, 2628CD, The Netherlands, and also with the Department of Electrical Engineering, Ferdowsi University of Mashhad, Mashhad, Iran (e-mail: rlotfi@ieee.org).

Digital Object Identifier 10.1109/TCSI.2014.2374852

PhADC-based demodulators have proven to have bit-error-rate (BER) characteristics close to an ideal coherent GFSK demodulator [4]. PhADCs based on a zero-crossing conversion algorithm have been realized in silicon by a resistor-bridge-based approach [5], [6] as well as a current-mirror-based approach [7], [8]. The benefits of robustness to circuit nonidealities and noise and large amplitude dynamic range of the resistor-bridge-based zero-crossing (ZC) PhADC has been addressed in [9]. Moreover, an IQ-assisted algorithm has recently been proposed and implemented in a charge-redistribution PhADC, resulting in a very energy-efficient PhADC topology [10].

However, though being a promising alternative to the IQ ADC for low power wireless receivers, there is a lack of thorough and accurate analysis of the fundamental benefits and limitations of the PhADC over the IQ ADC in the literature. In this paper, analytical methods to compare the PhADC and the IQ ADC are presented, aiming to provide deeper insights into their performance and to help designers make an optimum choice between them at system level. Phase signal-to-noise ratio (SNR) is proposed to facilitate the comparison of the PhADC and IQ ADC. The phase SNR is analytically related to the resolutions in phase and amplitude for the PhADC and the IQ ADC, respectively. The principal advantages and disadvantages of the PhADC are then accurately formulated or addressed with the aid of several implementation examples of the PhADC and the IQ ADC. Furthermore, the influence of the amplitude nonidealities on the phase is quantified for the PhADC and compared with the IQ ADC if necessary. It should be noted that we focus on the ZC PhADC in this paper rather than the charge-redistribution PhADC, but most of the analysis is independent from the conversion algorithms and the circuit architectures, i.e., valid for both PhADCs. We hereafter assume the PhADC is a ZC PhADC unless otherwise noted.

This paper is organized as follows. In Section II, the relationship between phase SNR and IQ amplitude resolution of the IQ ADC is derived for input vectors with constant and non-constant magnitudes, respectively. In Section III, the same analysis is applied to the PhADC and the phase SNR is related to the phase resolution as well. Section IV compares the PhADC and the IQ ADC from several different perspectives. In Section V, the effect of amplitude nonidealities on the PhADC are analyzed and compared with the IQ ADC. Phase-domain IQ amplitude mismatch and IQ offset detection techniques are also proposed and verified principally. Section VI summarizes the findings of this paper.

II. PHASE SNR OF IQ ADC

Analog baseband frequency/phase modulated I and Q signals are usually quantized by an IQ ADC, and then mapped onto phases in the digital domain during or before the phase demodulation. While the I and Q amplitude ADCs are characterized in

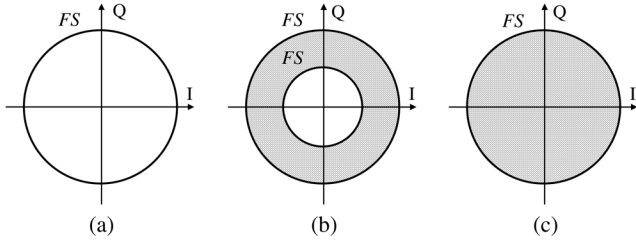


Fig. 1. Vector distribution with random phase and (a) constant magnitude, (b) random magnitude within $[FS/4, FS/2]$, and (c) random magnitude within $[0, FS/2]$.

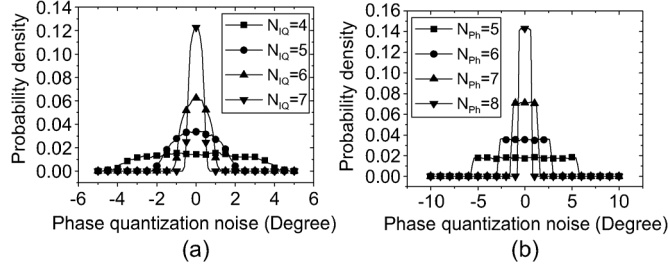


Fig. 2. Phase quantization noise PDF of (a) an IQ ADC for $N_{IQ} = 4, 5, 6,$ or 7 and a constant input vector magnitude, and (b) a PhADC for $N_{Ph} = 5, 6, 7,$ or 8 and a constant input vector magnitude.

the amplitude domain separately, it is more meaningful to characterize them together in the phase domain since eventually the phase is the only quantity processed by the phase demodulator. Therefore, the phase quantization noise introduced by the IQ amplitude quantization noise is analyzed here.

The phase quantization noise can be accurately formulated by a mathematical procedure as follows. Assuming the I amplitude quantization noise is uncorrelated with the I signal and so is its Q counterpart, the amplitude of the quantization noise are approximately uniformly distributed and spread more or less as white noise over the Nyquist bandwidth from dc to $f_s/2$ [11], where f_s is the sampling frequency. The phase quantization noise then becomes:

$$e(i, q, \Delta i, \Delta q) = \arctan \frac{q + \Delta q}{i + \Delta i} - \arctan \frac{q}{i}, \quad (1)$$

where i and q are the amplitudes of the I and Q signals, and Δi and Δq are the quantization noise terms superposed on them, respectively. The power of the phase error is given by [12]:

$$P_{\varphi, QN} = \iiint \iiint e(i, q, \Delta i, \Delta q)^2 \cdot f(\Delta i, \Delta q) \cdot d\Delta i \cdot d\Delta q \cdot di \cdot dq, \quad (2)$$

where $f(\Delta i, \Delta q)$ is the joint distribution density function of Δq and Δi , which both have a uniform probability density function (PDF). However, since the integration result of (2) is complicated and it does not provide any intuitive insight, a simulation-based approach is employed here instead. Moreover, the phase quantization noise power is highly dependent on the distribution of the vector magnitudes. Two scenarios with different vector magnitude distributions are analyzed, i.e., a constant magnitude distribution and a random magnitude distribution within a certain range.

A. Constant Vector Magnitude

A vector signal (i.e., a pair of I and Q signals) with constant magnitude $FS/2$ but random phase as shown in Fig. 1(a), is applied to an N_{IQ} bit IQ ADC with an amplitude least significant bit LSB_{IQ} . Following the quantization process of the i and q , the quantized amplitudes are converted to a quantized phase φ_{IQ} .

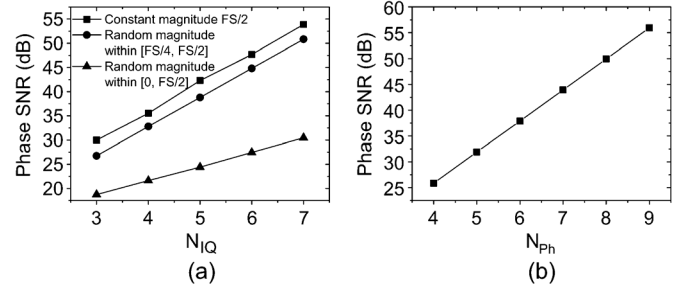


Fig. 3. (a) Phase SNR of an IQ ADC as a function of amplitude resolution N_{IQ} for different vector magnitude distributions. (b) Phase SNR of a PhADC as a function of phase resolution N_{Ph} ; the phase SNR is not affected by the vector magnitude variations.

While amplitude quantization noise Δq and Δi are uniformly distributed over $[-LSB_{IQ}/2, LSB_{IQ}/2]$, the phase quantization noise $e_{\varphi, IQ}$ introduced by Δq and Δi is not distributed in the same way due to the nonlinear amplitude-to-phase conversion as indicated by (1). This indeed can be observed in Fig. 2(a), which plots the PDF of the phase quantization noise when the input signal has constant magnitude but random phase. It is also confirmed by simulations that the phase quantization noise PDF is uncorrelated with the input phase when the input phase spans the entire phase range, i.e., $[0, 2\pi]$.

The SNR of output phase φ_{IQ} can now be calculated assuming input phase $\varphi_{IQ, in}$ is a full-scale sine wave:

$$\varphi_{IQ, in} = \pi \sin(2\pi ft). \quad (3)$$

The rms value of the input phase is therefore:

$$\varphi_{IQ, in, rms} = \frac{\pi}{\sqrt{2}}. \quad (4)$$

The phase SNR for an ideal N_{IQ} bit IQ ADC is therefore:

$$SNR_{\varphi, IQ} = 20 \log_{10} \frac{\varphi_{IQ, in, rms}}{e_{\varphi, IQ, rms}} \text{ (dB)}, \quad (5)$$

where $e_{\varphi, IQ, rms}$ is the rms value of the phase quantization noise, which can be determined by simulations. As shown by the upper curve in Fig. 3(a), $SNR_{\varphi, IQ}$ linearly increases with N_{IQ} , which can be fitted to a linear function as:

$$SNR_{\varphi, IQ} = 6N_{IQ} + 11.9 \text{ (dB)}. \quad (6)$$

The SNR of an amplitude ADC is usually quantified by a more intuitive metric, i.e., effective number of bits (ENOB) according to:

$$ENOB = \frac{SNR \text{ (dB)} - 1.76}{6.02}. \quad (7)$$

A similar concept can be applied to $SNR_{\varphi, IQ}$, yielding:

$$ENOB_{\varphi, IQ} = \frac{6}{6.02} N_{IQ} + 1.69 \approx N_{IQ} + 1.69, \quad (8)$$

which shows that phase ENOB is 1.69 bit greater than N_{IQ} for a constant-magnitude vector. However, realistic vector signals do not always have constant magnitudes. The phase SNR for a non-constant magnitude vector will be studied next.

B. Non-Constant Vector Magnitude

The vector magnitude in a practical receiver system might change with time-varying transmitting power and communication channel attenuation. As illustrated in Fig. 4(a), the amplitude quantization noise ($\Delta i, \Delta q$) produces a larger phase quantization noise ($\Delta \varphi_1$) at a small vector magnitude (A_1) than it does at a large vector magnitude, i.e., $\Delta \varphi_0$ associated with A_0 .

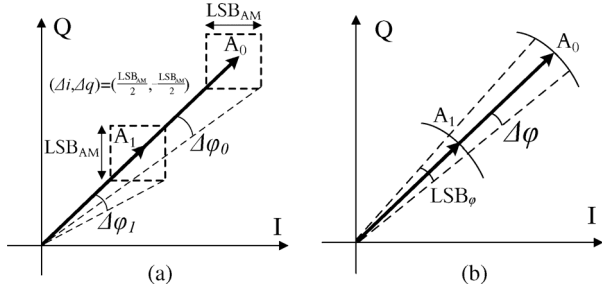


Fig. 4. Phase quantization noise when the input vector has different magnitudes for (a) an IQ ADC, and (b) a PhADC.

Thus, the total phase quantization noise power associated with a non-constant vector magnitude is greater than that associated with a constant vector magnitude.

Let us consider the two vector distributions shown in Fig. 1(b) and (c), which both have random phase distributions and random vector magnitudes, but with different magnitude ranges, i.e., $[FS/4, FS/2]$ in (b) and $[0, FS/2]$ in (c), respectively. Since the vector magnitude is usually maintained within a limited range by a preceding variable gain amplifier (VGA) in practice, the vector distribution shown in Fig. 1(b) is more realistic and representative than Fig. 1(a) and Fig. 1(c). The SNR of the quantized phase is calculated and plotted in Fig. 3(a), indicating that the phase SNR decreases with increasing magnitude range. For the vector distribution shown in Fig. 1(b), a linear function can relate the phase SNR and N_{IQ} as:

$$\text{SNR}_{\varphi, IQ, NM} = 6N_{IQ} + 8.7(\text{dB}). \quad (9)$$

Thus, the ENOB of the phase output is:

$$\text{ENOB}_{\varphi, IQ, NM} \approx N_{IQ} + 1.2. \quad (10)$$

The key observation from comparing (8) and (10) is that 0.49 bit phase ENOB is lost due to the increased magnitude range. In other words, an IQ ADC needs 0.49 bit extra to accommodate the varying vector magnitude and compensate for the phase ENOB degradation.

III. PHASE SNR OF PHADC

Before comparing the phase SNR of a PhADC with that of an IQ ADC, phase SNR of the PhADC also needs to be related to phase resolution analytically for different vector magnitude distributions. This will be discussed in this section.

A PhADC is an amplitude-to-phase converter with quantization functionality. For an N_{Ph} bit PhADC, the IQ-plane is split into $2^{N_{Ph}}$ sectors with an angle of $\text{LSB}_{\varphi} = 2\pi/2^{N_{Ph}}$ between consecutive quantization intervals [7], as illustrated by the example in Fig. 5(a). The quantization is realized by generating and then detecting the signs (zero crossings) of the original and rotated I or Q projections. As shown in Fig. 5(b), the Q projection of vector A_0 and its rotated versions are $q_{0,1,\dots,7}$, respectively. The 4 bit PhADC senses the zero crossings of $q_{0,1,\dots,7}$, and counts the number of positive and negative zero crossings induced, then estimates the phase of A_0 ; the greater the number of the rotated projections, the higher the resolution of the phase. This quantization process can be seen in such a way that several input-dependent (unknown) quantization levels (e.g., $q_{0,1,\dots,7}$) are generated to compare with zero (known) amplitude, which is opposite to the usual amplitude quantization process, i.e., several reference (known) quantization levels are generated to quantize an unknown input amplitude. However, in essence, both quantization processes are comparisons of one amplitude

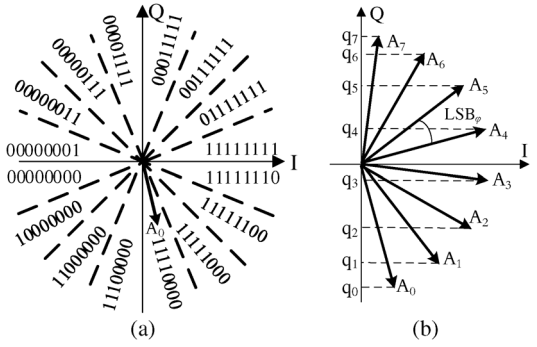


Fig. 5. (a) The complex IQ plane is split into 16 uniform sectors by a 4 bit PhADC. (b) The Q projection of a vector A_0 and its seven rotated versions; the 8-bit words in (a) represent the signs (zero-crossing detections) of the 8 Q projections when the vector is in the corresponding phase sector.

with several other amplitudes. This similarity can help us understand the influence of comparator offsets on the PhADC performance, as will be discussed in Section V.

A rotated projection q_k is related to the fundamental projections i_0 and q_0 as follows [4], [7]:

$$q_k = i_0 \cdot \sin \frac{k\pi}{2^{N_{Ph}-1}} + q_0 \cdot \cos \frac{k\pi}{2^{N_{Ph}-1}}, k = 0, 1, \dots, 2^{N_{Ph}-1} - 1. \quad (11)$$

This linear combination function can be implemented in circuitry either by a resistive bridge that converts input currents to phase-shifted voltages [5], [6], or a weighted current array that converts input voltages to phase-shifted currents [7].

Being a linear quantizer in the phase domain, the quantization noise of the PhADC has properties similar to that of a linear amplitude ADC. It is accurate enough for most amplitude ADCs that the amplitude quantization noise for any ac signal that spans more than a few LSBs can be approximated by an uncorrelated sawtooth waveform having a peak-to-peak value of one LSB [13]. This assumption also holds true for the PhADC when the input phase spans the entire phase range, i.e., $[0, 2\pi)$. Fig. 2(b) shows the PDF of the phase quantization noise for a constant-magnitude input signal with random phase. Unlike the Gaussian-like distribution as shown in Fig. 2(a), the phase quantization noise is uniformly distributed over $[-\text{LSB}_{\varphi}/2, \text{LSB}_{\varphi}/2]$. The root-mean-square phase quantization noise is:

$$e_{\varphi, Ph, rms} = \frac{\text{LSB}_{\varphi}}{\sqrt{12}}. \quad (12)$$

Assuming the input phase is a full-scale sine wave expressed by (3) with an rms value given by (4), the SNR of the quantized phase is:

$$\text{SNR}_{\varphi, Ph} = 6.02N_{Ph} + 1.76(\text{dB}). \quad (13)$$

Hence, the ENOB of the PhADC is:

$$\text{ENOB}_{\varphi, Ph} = N_{Ph}. \quad (14)$$

(13) is also well matched with the simulation results shown in Fig. 3(b), in which $\text{SNR}_{\varphi, Ph}$ is plotted versus the phase resolution N_{Ph} .

To be consistent with the analysis applied to the IQ ADC, the phase quantization noise distribution and the phase SNR need to be analyzed in case the input vector magnitude is not constant as well. Since the PhADC is a direct linear quantizer in the phase domain, the phase quantization noise is independent from the vector magnitude. This independence is also conceptually illustrated in Fig. 4(b), showing that a large vector A_0 has

the same phase quantization error as a small vector A_1 . Therefore, (12), (13) and Fig. 3(b) also hold true for an input vector with a random magnitude and a random phase. Also, the phase quantization noise follows the same uniform distribution as the ones shown in Fig. 2(b).

The analysis in this section and Section II suggests that the phase SNR of an IQ ADC decreases with increasing vector magnitude range, whereas that of a PhADC is immune to the vector-magnitude variation. In other words, from a system perspective, the IQ ADC needs extra bit to accommodate the varying vector magnitude, or the preceding automatic gain control (AGC) needs a finer gain resolution, whereas the PhADC can inherently accommodate the variation and relax the AGC control. This is one of fundamental benefits of the PhADC over the IQ ADC. This benefit has also been proven by measurement results in [6], [7], [10] and summarized in [10] by the authors.

IV. PHADC AND IQ ADC COMPARISON

The foregoing analysis formulates the vector-magnitude-variation accommodation effect of the PhADC. In this section, further comparisons between the two ADCs are made from several other perspectives. In IQ ADC-based low power receivers, moderate resolution (6–9 bit) and moderate speed (2.4–8 MS/s) SAR and pipeline ADCs are typically employed [14]–[16]. By contrast, PhADC-based low power receivers incorporate low phase resolution (4–5 bit) and moderate speed (1–20 MS/s) PhADCs [6], [7], [10]. We make the following observations on these two scenarios:

- 1) Embedded demodulation. While the IQ ADC needs subsequent digital demodulation, the PhADC embeds most of the demodulation process in the quantization, thus saving the power and the area otherwise needed for the demodulation.
- 2) Vector-magnitude variation accommodation. The 6–9 bit amplitude resolution of an IQ ADC can be translated into a phase $\text{ENOB}_{\varphi, \text{IQ}}$ of 7.7–10.7 bit as indicated by (8), which is more than that required by the FSK/PSK demodulation defined in low power wireless standards, e.g., BLE. This extra dynamic range is used to accommodate vector magnitude variations and interference. In contrast to the IQ ADC, a PhADC can inherently accommodate the magnitude variation as described in Section III, and hence no extra phase dynamic range is needed for a PhADC.
- 3) Interference accommodation. As mentioned above, the IQ ADC usually allocates some extra dynamic range to accommodate interference besides the magnitude variations, hence the desired channel can be precisely selected in the digital domain if the interference is not sufficiently suppressed by the stages preceding the ADC. However, the PhADC is not able to accommodate the interference even with extra phase dynamic range. This is because the amplitude interference is nonlinearly translated into a phase error of the desired phase, and the desired phase and the phase error are no longer carried by well-separated frequency channels as the desired amplitude and the interference at the input of the PhADC. These different attributes of interference accommodation marks an important application boundary between the two ADCs. That is, the PhADC is a more compact quantization and demodulation solution due to its embedded demodulation attribute, while the IQ ADC-based receiver can provide more channel-selection flexibility. For example, a simple 3rd-order analog channel

selection filter and a 4 bit PhADC can already satisfy the requirements of the BLE standard [8], while IQ ADC-based receivers can accommodate multiple low power wireless standards [15], [16].

- 4) Energy efficiency. After many decades of research, today's IQ ADCs have become quite energy efficient in advanced IC processes. As an example, a SAR ADC in 40 nm technology offers today with a figure of merit (FoM) of 0.85 fJ/conv. step [17]. By contrast, the emerging PhADC has only a few reported silicon realizations and a state-of-the-art FoM of 1.2 pJ/conv. step in 0.18 μm technology [10]. Although the reported PhADCs are not as energy efficient as the IQ ADC yet, we want to address the fundamental energy difference between them, hence showing the room for improvement we could explore.

The following comparison will be made in the typical operating condition of a PhADC, i.e., low phase resolution (4–5 bit) with no need to accommodate the interference, demonstrating the preferable one of the two ADCs in such condition. The translated amplitude resolution requirement of the IQ ADC is about 3–4 bit, as indicated by (10), which is less than that of the IQ ADCs in [14]–[16] (6–9 bit) since no interference need to be accommodated. This low resolution requirement makes flash, SAR, and pipeline all possible architectures for the IQ ADC since they have the same order of energy efficiency [18]. The flash architecture is selected in the comparison due to its similarity with the most common PhADC architecture, i.e., the ZC PhADC [6], [7]. Since the majority of the power consumption of both a flash ADC and a ZC PhADC are attributed to the comparators, the number of comparators is used to specify the power consumption. Also, the sampling rate and the input signals of both the two ADCs are assumed to be the same.

An N_{IQ} bit classical flash ADC has $2^{N_{\text{IQ}}} - 1$ comparators, thus an IQ ADC with two N_{IQ} bit ADCs has $2(2^{N_{\text{IQ}}} - 1)$ comparators. As described in Section III, an N_{Ph} bit PhADC has $2^{N_{\text{Ph}} - 1}$ thresholds, so $2^{N_{\text{Ph}} - 1}$ comparators. If the IQ ADC and the PhADC have the same number of comparators, they have a resolution relationship as follows:

$$N_{\text{Ph}} = \log_2(2^{N_{\text{IQ}}} - 1) + 2, \quad (15)$$

indicating that N_{Ph} is roughly 2 bits larger than N_{IQ} .

As noted in Section II-B, the non-constant vector distribution shown in Fig. 1(b) is more realistic and representative than Fig. 1(a) and Fig. 1(c). Thus, the following comparison is made for an input vector with non-constant magnitude between $FS/4$ and $FS/2$. $\text{ENOB}_{\varphi, \text{IQ}, \text{NM}}$ and $\text{ENOB}_{\varphi, \text{Ph}}$ of the IQ ADC and the PhADC are given by (10) and (14), respectively. Given the same number of comparators, i.e., their resolutions meet (15), the ENOB difference is:

$$\text{ENOB}_{\varphi, \text{Ph}} - \text{ENOB}_{\varphi, \text{IQ}, \text{NM}} = \log_2(2^{N_{\text{IQ}}} - 1) - N_{\text{IQ}} + 0.8, \quad (16)$$

showing that $\text{ENOB}_{\varphi, \text{Ph}}$ is higher than $\text{ENOB}_{\varphi, \text{IQ}, \text{NM}}$ as long as $N_{\text{IQ}} > 1$ bit. For example, ENOB difference is 0.7 bit when $N_{\text{IQ}} = 4$ (i.e., both ADCs have 30 comparators). For another example, if both ADCs have a phase ENOB of 5 bit, the IQ ADC and the PhADC need 26 and 16 comparators ($N_{\text{IQ}} = 3.8$ and $N_{\text{Ph}} = 5$), respectively. Thus, the PhADC has a lower theoretical energy limit (fewer comparators) than the flash IQ ADC for a given phase ENOB. The favorable energy efficiency of the PhADC is contributed by two facts: 1) immunity to vector-magnitude variation, and 2) 1-D (phase-only) quantization rather than 2-D (IQ) quantization.

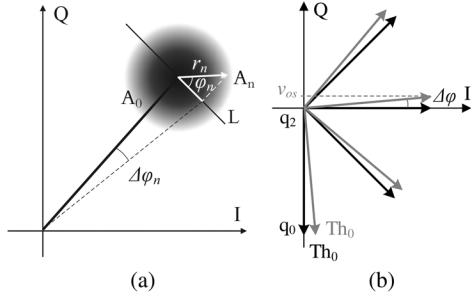


Fig. 6. (a) Phase noise caused by complex Gaussian amplitude noise. (b) Phase reference level fluctuation caused by comparator offsets for a 3 bit PhADC.

In summary, compared to the IQ ADC, the PhADC, due to its embedded demodulation attribute, is a more compact quantization and demodulation solution when interference accommodation is not required. Moreover, in the typical operating condition of the PhADC, i.e., low phase resolution with no need to accommodate the interference, the theoretical energy limit of the PhADC is addressed with respect to the IQ ADC. Considering a flash ADC as an example of the low resolution (3-4 bit) IQ ADC, the PhADC has a lower theoretical energy limit than the flash IQ ADC for a given phase ENOB due to the immunity to magnitude variation and the phase-only quantization, illustrating the great room for energy efficiency improvement that the emerging PhADC has.

V. PHASE NONIDEALITIES DUE TO AMPLITUDE NONIDEALITIES

Our analysis thus far only takes into account the quantization noise, but no other amplitude nonidealities, which usually manifest themselves as noise, gain errors, and offsets injected by preceding stages, as well as the amplitude errors introduced during conversions. Due to the different quantization mechanism of the PhADC with respect to that of an IQ ADC, the influence of the amplitude nonidealities on the phase should be analyzed and compared with the IQ ADC if necessary. The amplitude errors introduced during conversions highly depend on the circuit architecture of the PhADC. We focus on the effects of comparator offset of the ZC PhADC here.

A. Input Noise

Since all noise introduced before ADCs affects the phase SNR of both an IQ ADC and a PhADC in the same manner, the analysis below will first take the IQ ADC as an example and then simply extend the conclusions to the PhADC. Assuming the input noise of both I and Q signals are white Gaussian noise with zero mean and a standard deviation σ_{noise} , a vector A_0 and its complex Gaussian noise are shown in Fig. 6(a). r_n is the magnitude of the noise vector and φ_n is its phase with respect to line L (perpendicular to A_0) in the figure. Using a small angle approximation, the phase noise $\Delta\varphi_n$ introduced by noise vector A_n can be approximated as:

$$\Delta\varphi_n \approx \tan \Delta\varphi_n = \frac{r_n \cos \varphi_n}{FS/2}. \quad (17)$$

The noise magnitude r_n and noise phase φ_n of the complex Gaussian noise have Rayleigh and uniform distributions respectively, and they are statistically independent of each other [12]. The power of the phase noise is given by [12]:

$$P_{\varphi,\text{noise}} = \int_0^{+\infty} \int_{-\pi}^{\pi} \left(\frac{r_n \cos \varphi_n}{FS/2} \right)^2 f(r_n, \varphi_n) d\varphi_n dr_n, \quad (18)$$

where $f(r_n, \varphi_n)$ is the joint density of r_n and φ_n . The density functions of r_n and φ_n are:

$$f(r_n) = \frac{r_n}{\sigma_{\text{noise}}^2} e^{-r_n/2\sigma_{\text{noise}}^2} \quad r_n \in [0, +\infty), \quad (19)$$

$$f(\varphi_n) = \begin{cases} 1/2\pi & \varphi_n \in (-\pi, +\pi) \\ 0 & \text{otherwise.} \end{cases} \quad (20)$$

Thus, the joint density function of r_n and φ_n is:

$$f(r_n, \varphi_n) = \frac{r_n e^{-\frac{r_n}{2\sigma_{\text{noise}}^2}}}{\sigma_{\text{noise}}^2} \frac{1}{2\pi}, \quad r_n \in [0, +\infty), \varphi_n \in (-\pi, +\pi). \quad (21)$$

Substituting (21) into (18), we get:

$$P_{\varphi,\text{noise}} = \frac{\sigma_{\text{noise}}^2}{(FS/2)^2} = \frac{P_{\text{am},\text{noise}}}{(FS/2)^2}, \quad (22)$$

where $P_{\text{am},\text{noise}}$ is the amplitude noise power. Since $P_{\varphi,\text{noise}}$ is independent of the phase of A_0 , the average phase noise power over the entire phase range is still (22) as long as the vector magnitude is constant. It is reasonable to assume that the amplitude quantization noise is uncorrelated with the input amplitude and so is its phase counterpart, as noted in Section II; thus both the IQ amplitude and phase are assumed to be sinusoidal. The power of the IQ amplitude is $P_{\text{IQ},\text{sig}} = (FS/2)^2/2$. If the SNR of the IQ signal is defined as $\text{SNR}_{\text{am}} = P_{\text{IQ},\text{sig}}/P_{\text{am},\text{noise}}$, (22) can be rewritten as:

$$P_{\varphi,\text{noise}} = \frac{1}{2\text{SNR}_{\text{am}}}. \quad (23)$$

If quantization noise is not taken into account, SNR is:

$$\text{SNR}_{\varphi,\text{noise}} = \frac{P_{\varphi}}{P_{\varphi,\text{noise}}} = \frac{\pi^2/2}{1/(2\text{SNR}_{\text{am}})} = \pi^2 \text{SNR}_{\text{am}}, \quad (24)$$

where P_{φ} is the phase signal power. It can also be expressed in dB as:

$$\text{SNR}_{\varphi,\text{noise}} = \text{SNR}_{\text{am}} + 10 \text{ (dB)}. \quad (25)$$

The total SNR with quantization noise and $P_{\varphi,\text{noise}}$ is:

$$\text{SNR}_{\text{IQ},\varphi,\text{TN}} = \frac{1}{1/\text{SNR}_{\text{IQ},\varphi} + 1/\text{SNR}_{\varphi,\text{noise}}}, \quad (26)$$

where $\text{SNR}_{\text{IQ},\varphi}$ is given by (6). $\text{SNR}_{\text{IQ},\varphi,\text{TN}}$ can be rewritten as a function of SNR_{am} and N_{IQ} by substituting (6) and (24) into (26), resulting in:

$$\text{SNR}_{\text{IQ},\varphi,\text{TN}} = \frac{\pi^2 \text{SNR}_{\text{am}}}{\pi^2 \text{SNR}_{\text{am}} 10^{-(0.6N_{\text{IQ}}+1.19)} + 1}. \quad (27)$$

The above analysis also holds true for the PhADC if the $\text{SNR}_{\text{IQ},\varphi}$ in (26) is replaced by (13), thus the phase SNR of the PhADC considering both the quantization noise and the phase noise is:

$$\text{SNR}_{\text{Ph},\varphi,\text{TN}} = \frac{\pi^2 \text{SNR}_{\text{am}}}{\pi^2 \text{SNR}_{\text{am}} 10^{-(0.602N_{\text{Ph}}+0.176)} + 1}. \quad (28)$$

The accuracies of (27) and (28) are verified by simulations using a 4 bit IQ ADC and a 6 bit PhADC respectively, as shown in Fig. 7(a). The difference between the calculations and simulations is less than 0.5 dB, and is caused by the small angle approximation.

In summary, if both the IQ ADC and the PhADC are limited by the input noise rather than the quantization noise, their phase SNR is 10 dB higher than SNR_{am} as shown by (25). When the phase quantization noise is taken into account, the quantization noise becomes more dominant than the input noise with increasing SNR_{am} . In the given example, $\text{SNR}_{\text{IQ},\varphi,\text{TN}}$

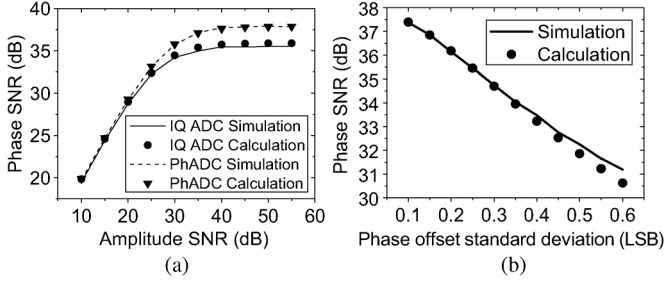


Fig. 7. (a) Phase SNR as a function of amplitude SNR for a 4 bit IQ ADC and a 6 bit PhADC. (b) SNR degradation due to comparator offsets for a 6 bit PhADC.

and $\text{SNR}_{\text{Ph},\varphi,\text{TN}}$ are not limited by SNR_{am} anymore when SNR_{am} is larger than 30 dB.

B. Comparator Offsets

Let us first consider the effect of comparator offset in a standard flash ADC. The input-referred offset of a comparator consists of static components (e.g., threshold mismatch of an input pair), as well as dynamic components caused by the nonlinear transconductance of the latches. It is usually acceptable to characterize the offset by a Gaussian distribution with zero mean and a standard deviation σ_{OS} [11]. The fluctuation of reference levels caused by the comparator offset in a flash amplitude ADC can be seen as a random noise source in series between the input signal and an ideal quantizer if the input signal is assumed to vary sufficiently [11]. Thus, a flash ADC can be modeled as an ideal quantizer with an input as:

$$v_{\text{in,OS}} = v_{\text{in}} + v_{\text{OS}}, \quad (29)$$

where v_{in} is the input signal, and v_{OS} is the comparator offset with a standard deviation σ_{OS} .

We now determine the effects of comparator offsets on the PhADC. As noted in Section III, an N_{Ph} bit PhADC can be seen as an amplitude quantizer with $2^{N_{\text{Ph}}-1}$ unknown quantization levels, which are all compared with a known zero amplitude (i.e., zero-crossing detection). This is similar to a flash amplitude ADC, which instead has multiple known quantization levels and an unknown input. Therefore, it is also valid to assume that the PhADC with comparator offsets behaves as an ideal PhADC with a Gaussian distributed “zero” amplitude as:

$$\text{zero}_{\text{OS}} = 0 + v_{\text{OS}}. \quad (30)$$

The phase noise introduced by v_{OS} can be conceptually explained by an example in Fig. 6(b) as follows. $q_{0,1\dots3}$ are the original and three rotated Q projections of phase quantization level $Th_0 = -\pi/2$, and the projection q_2 should ideally be zero. The Gaussian-“zero” amplitude makes q_2 fluctuate around zero, thus resulting in a fluctuation of Th_0 . If the fluctuation around zero is v_{OS} as shown in Fig. 6(b), the phase error on Th_0 is $\Delta\varphi = \arcsin(v_{\text{OS}}/(FS/2))$, which can be approximated using a small angle approximation as $\Delta\varphi = v_{\text{OS}}/(FS/2)$. Therefore, the overall effect of the comparator offsets is introducing Gaussian distributed phase offsets into all phase quantization levels, which now is exactly the same as the effect of the offsets on the flash amplitude ADC as discussed above. Moving the offsets of all quantization levels into an equivalent one in series with the input phase, the input becomes:

$$\varphi_{\text{Ph,OS}} = \varphi + \varphi_{\text{OS}}, \quad (31)$$

where φ_{OS} has a Gaussian distribution with zero mean and a standard deviation $\sigma_{\varphi} = \sigma_{\text{OS}}/(FS/2)$. The offset now plays

exactly the same role as the Gaussian noise discussed in Section V-A. Thus, the power of φ_{OS} is:

$$P_{\text{Ph},\varphi,\text{OS}} = \frac{\sigma_{\text{OS}}^2}{(FS/2)^2}, \quad (32)$$

If the quantization noise is not taken into account, SNR becomes:

$$\text{SNR}_{\text{Ph},\varphi,\text{OS}} = \frac{P_{\varphi}}{P_{\text{Ph},\varphi,\text{OS}}} = \frac{(\pi FS)^2}{8} \frac{1}{\sigma_{\text{OS}}^2}. \quad (33)$$

Replacing $\text{SNR}_{\varphi,\text{noise}}$ and $\text{SNR}_{\text{IQ},\varphi}$ in (26) with $\text{SNR}_{\text{Ph},\varphi,\text{OS}}$ and (13), the total SNR with quantization noise is:

$$\text{SNR}_{\text{Ph},\varphi,\text{QN+OS}} = \frac{\pi^2}{\pi^2 10^{-(0.602N_{\text{Ph}}+0.176)} + 2\sigma_{\varphi}^2}. \quad (34)$$

The accuracy of (34) is verified by the simulation results shown in Fig. 7(b), which indicate that a small angle approximation is less valid at higher offset values, but the approximation error is still less than 0.5 dB.

The key observation in the above analysis is that the effect of the comparator offsets can be modeled as a phase noise with a Gaussian distribution at the input and be formulated as (34).

C. IQ Offsets and IQ Amplitude Mismatch

The above analysis shows that the noise has the same effect on an IQ ADC as on a PhADC. However, two other amplitude nonidealities, i.e., IQ offset and IQ amplitude mismatch behave differently in the two ADCs, as will be described next.

Due to the nonlinear amplitude-to-phase conversion, IQ offsets and amplitude mismatch can produce nonlinear phase distortions. Although theoretically both the IQ ADC and PhADC suffer from this effect in the same way, it is well known in practice that the mismatch and the offset can be detected and calibrated if necessary before amplitude is converted into phase for the IQ ADC, whereas the direct mismatch and offset detection cannot be employed for the PhADC due to the absence of amplitude information. Therefore, the effects of phase nonlinearity are only analyzed for the PhADC.

An ideal PhADC has a linear transfer function, as the curve TF'_1 shows at the right hand side of Fig. 8(a), resulting in a circular output trajectory centered exactly at the origin of the IQ plane for a constant-magnitude input vector, as depicted at the left hand side of the figure. When an positive offset v_{OS} is added to the I amplitude, the trajectory is shifted to the right and the corresponding phase transfer function changes to the nonlinear curve TF''_1 . Similarly, the nonlinear transfer function caused by a Q offset with a value of v_{OS} is shown in Fig. 8(b), which has the same shape as the one in Fig. 8(a) but with a phase shift of $\pi/2$. It is readily expected that TF''_1 is an odd-order nonlinear function with a maximum integral nonlinearity (INL) of INL_{max} , whereas TF'_Q has both even-order and odd-order nonlinear terms albeit with the same INL_{max} . The difference of TF''_1 and TF'_Q shows that I and Q offsets have different effects on the phase distortion when the two-dimensional vector is mapped onto the one-dimensional phase.

A formal analysis can be carried out to derive the nonlinear transfer functions of TF''_1 and TF'_Q and then calculate the total harmonic distortion (THD) and INL_{max} , which can specify the nonlinearity in a static and dynamic manner, respectively. However, as we will see, none of nonlinear terms is much more prominent than the other when the input phase full scale is 2π , thus a simplification to a few dominant nonlinear terms doesn't

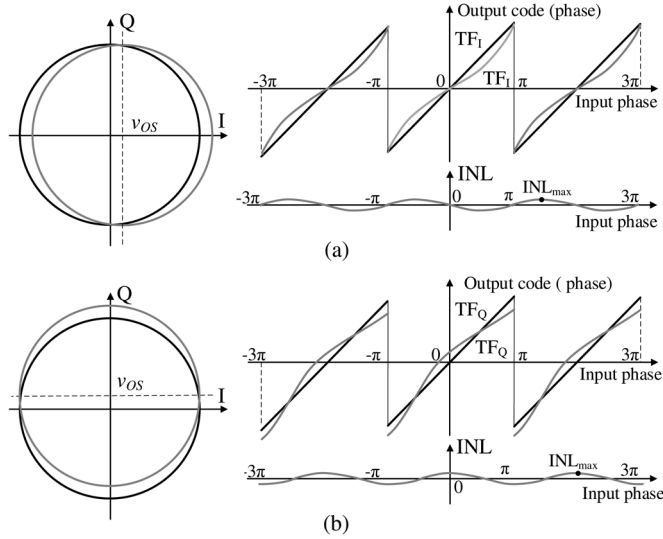


Fig. 8. Vector trajectory shifting and nonlinear phase transfer functions due to (a) I offset, and (b) Q offset. The shape of TF'_I and TF'_Q are verified using Matlab simulations and redrawn in the figure.

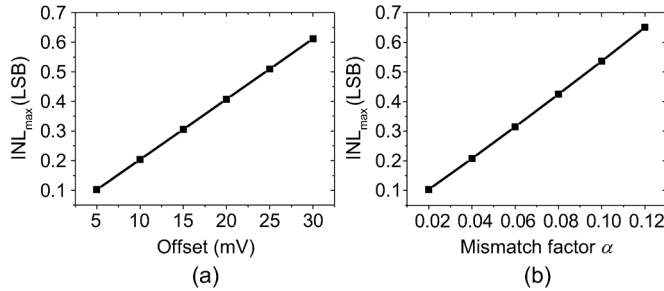


Fig. 9. INL_{max} as a function of (a) I or Q offset, and (b) mismatch factor α . The full scale of I and Q signals is 1 V. A 6 bit PhADC is assumed.

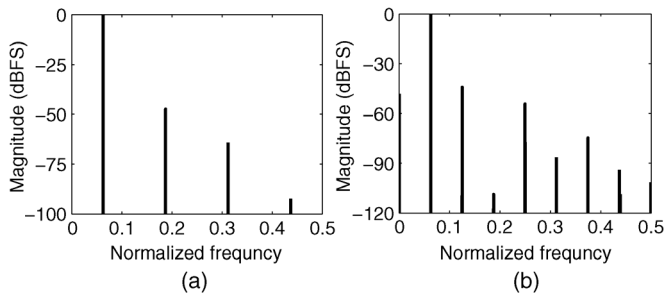


Fig. 10. Example of phase harmonic distortions due to (a) I offset (10 mV), and (b) Q offset (10 mV). The full scale of I and Q signals is 1 V. Phase quantization noise is not taken into account.

have sufficient accuracy. Therefore, we must resort to simulations to verify the effect of the IQ offset on the INL_{max} and THD.

The INL_{max} of TF'_I and TF'_Q is the same, and Fig. 9(a) shows that INL_{max} increases with the offset for a 6 bit PhADC. When the nonlinearity is quantified in a dynamic manner with a 2π full-scale sinusoidal input phase, the output spectrum is shown in Fig. 10 for a PhADC with an I offset and a Q offset, respectively. The spectrum shows that the I offset only introduces odd-order nonlinearity whereas the Q offset introduces both even and odd-order nonlinearities. Moreover, a Q offset gives rise to greater nonlinearity distortions than an I offset with

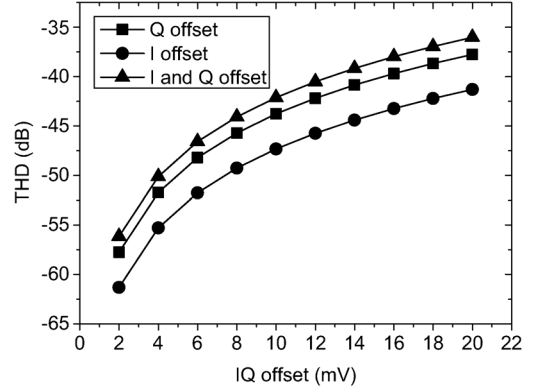


Fig. 11. THD as a function of I and Q offsets. The full scale of I and Q signals is 1 V.

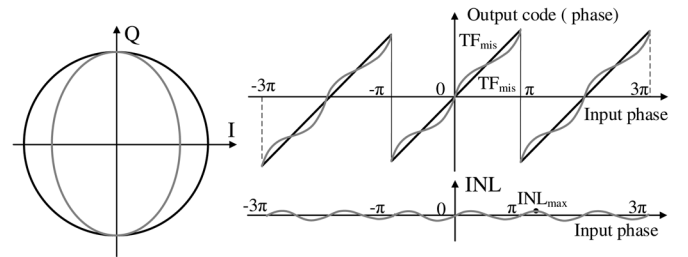


Fig. 12. Vector trajectory shifting and phase nonlinearities due to Q amplitude mismatch.

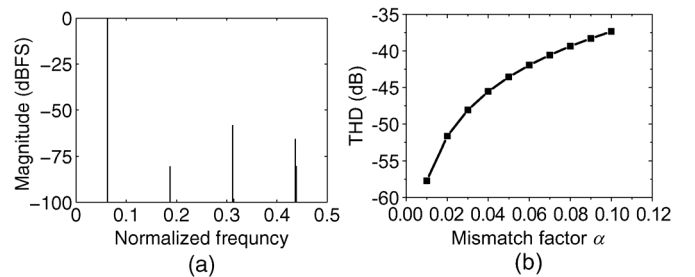


Fig. 13. (a) Example of phase harmonic distortion due to IQ amplitude mismatch ($\alpha = 0.01$). Phase quantization noise is not taken into account. (b) THD as a function of α .

the same value does, which can be observed in Fig. 11 showing THD as a function of the I and Q offset.

A similar analysis can also be applied to examine the effect of IQ amplitude mismatch. As shown in Fig. 12, when the I and Q full scale FS_I and FS_Q have a mismatch factor

$$\alpha = 1 - \frac{FS_I}{FS_Q}, \quad (35)$$

the vector trajectory is elliptical instead of circular, and the corresponding phase transfer function is an odd-order nonlinear curve TF'_{mis} with INL_{max} increasing with α [Fig. 9(b)]. The output spectrum of a PhADC suffering from the IQ amplitude mismatch is shown in Fig. 13(a) and the resulting THD is plotted versus mismatch factor α in Fig. 13(b).

Let us summarize our findings thus far. During the conversion of a two-dimensional vector to a one-dimensional phase, both offsets and mismatch of the amplitude can be transferred into nonlinearities of the phase. Moreover, a Q offset can give rise to more distortion than an I offset with the same value does. The nonlinearity asymmetry of I and Q offset deserves careful

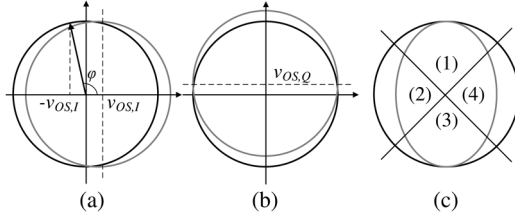


Fig. 14. Vector distribution imbalance caused by (a) I offset, (b) Q offset, and (c) IQ amplitude mismatch.

attention if the error of a phase signal is dominated by nonlinear distortion.

D. IQ Offsets and IQ Amplitude Mismatch Detection

The above analysis shows that nonlinearities introduced by offset and amplitude mismatch may significantly degrade the phase SNR of a PhADC, thereby dictating proper techniques to detect and calibrate the offset and the mismatch. A mixed-signal approach, i.e., detecting the offset and the mismatch in the digital domain and calibrate them in the analog domain is usually incorporated in a system with an IQ ADC. Similarly, a digital phase-domain detection principle is proposed for the PhADC as well in this section, offering a possibility for calibration in the analog domain.

The principle can be conceptually described by Fig. 14(a). Assume a circular vector trajectory is shifted to the right side of the complex plane by a positive I offset. In such a case, there are more vectors in the right half of the plane than in the left half if originally all vectors were evenly distributed along the circle. Therefore, the amplitude and sign of the I offset can be estimated by detecting the distribution density of the vectors in the right and left half planes. This principle holds also true for the Q offset when detecting the distribution density in the top and bottom half planes as shown in Fig. 14(b), as well as for the amplitude mismatch when detecting the density in Regions (1), (2), (3), and (4) as shown in Fig. 14(c). Thus, the amplitude mismatch and the offset detection can both be realized by a simple density analysis process in the digital domain without too much extra effort.

We now formulate the imbalance by taking the example of the I offset in Fig. 14(a). Due to the offset $v_{OS,I}$, phase φ_0 is now shifted to $\pi/2$, indicating that all vectors between $[-\varphi_0, \varphi_0]$ are now in the right half of the shifted vector circle. Hence, the distribution imbalance between the right and left half planes is:

$$\text{IMB}_{OS} = \frac{2\varphi_0}{2\pi} - \frac{2(\pi - \varphi_0)}{2\pi} = \frac{2\varphi_0}{\pi} - 1. \quad (36)$$

Substituting $\varphi_0 = (\pi/2) + \arcsin(v_{OS,I}/(FS/2))$ into (36), we get:

$$\text{IMB}_{OS} = 2 \arcsin \frac{v_{OS,I}}{FS/2} \pi \approx \frac{4v_{OS,I}}{\pi \cdot FS}. \quad (37)$$

This equation holds also true for the distribution imbalance between the top and bottom half planes if $v_{OS,I}$ is replaced by Q offset $v_{OS,Q}$.

Regarding the IQ amplitude mismatch, as shown in Fig. 14(c), its effect is the distribution imbalance between Regions (1) + (3) and Regions (2) + (4), denoted by IMB_{mis} . Similar calculations as (36) and (37) apply to IMB_{mis} and yields:

$$\text{IMB}_{\text{mis}} = 1 - \frac{4 \arctan(1 - \alpha)}{\pi}. \quad (38)$$

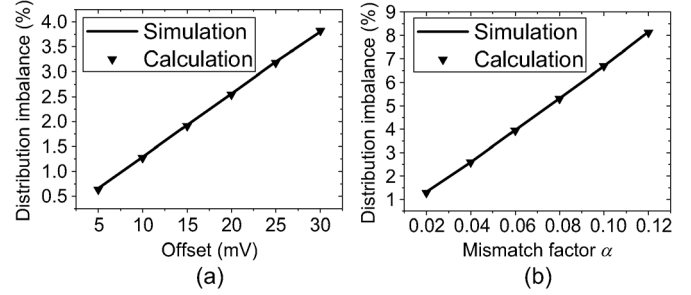


Fig. 15. Vector distribution imbalance as a function of (a) IQ offset (the full scale of I and Q signals is 1 V) and (b) IQ amplitude mismatch.

Simulation results in Fig. 15 show that the distribution imbalance increases with offsets and amplitude mismatch, which is consistent with (37) and (38).

The above analysis provides an effective approach to detect the IQ offset and the IQ amplitude mismatch in the digital domain, enabling the possibility to calibrate them in the analog domain, which is usually necessary in a receiver system. Note that, in order to calculate the absolute value of the offsets, one of FS_I and FS_Q should be available (the other one can be calculated from the known one, α and (35)), as indicated by (37). This can be accomplished by employing one auxiliary amplitude ADC in the calibration procedure.

VI. CONCLUSIONS

This paper presents a thorough comparison of PhADCs and IQ ADCs. In comparison with an IQ ADC, a PhADC, due to its embedded demodulation attribute, is a more compact quantization and demodulation solution when interference accommodation is not required. Moreover, considering a flash ADC as an example of the low resolution (3-4 bit) IQ ADC, the PhADC has a lower theoretical energy limit than the flash IQ ADC for a given phase ENOB due to the immunity to magnitude variation and the phase-only quantization, thereby showing the great room for energy efficiency improvement that the emerging PhADC has.

Explicit relationships between the input amplitude SNR and the output phase SNR for both ADCs have been formulated. The effect of the comparator offsets on the phase SNR has been derived for the PhADC. An important limitation of the PhADC is the phase nonlinearity stemming from IQ offset and IQ mismatch. In order to provide a cancellation possibility for the offset and mismatch, a simple mismatch and offset detection technique in the phase domain is proposed and then verified principally.

All of the analysis results provide deep and quantitative insights into the fundamental benefits and limitations of the PhADC over the IQ ADC, and prove that the PhADC is a promising quantization and demodulation solution for low power wireless receivers with phase modulations.

REFERENCES

- [1] E. K. B. Lee and H. M. Kwon, "New baseband zero-crossing demodulator for wireless communications. I: Performance under static channel," in *Proc. IEEE Military Commun. Conf. (MILCOM)*, Nov. 1995, pp. 543–547.
- [2] N. Dehaese, S. Bourdel, H. Barthelemy, Y. Bachelet, and G. Bas, "FSK zero-crossing demodulator for 802.15.4 low-cost receivers," in *Proc. IEEE Int. Conf. Electron., Circuits, Syst. (ICECS)*, Dec. 2005, pp. 1–4.
- [3] S. Masmoudi, A. Ghazel, and P. Loumeau, "Phase data converter design for IEEE 802.15.4-based wireless receiver," in *Proc. IEEE Int. Conf. Electron., Circuits, Syst. (ICECS)*, Dec. 2007, pp. 955–958.

- [4] S. Samadian, R. Hayashi, and A. A. Abidi, "Demodulators for a zero-IF Bluetooth receiver," *IEEE J. Solid-State Circuits*, vol. 38, no. 8, pp. 1393–1396, Aug. 2003.
- [5] E. Le Roux, N. Scolari, B. Banerjee, C. Arm, P. Volet, D. Sigg, P. Heim, J.-F. Perotto, F. Kaess, N. Raemy, A. Vouilloz, D. Ruffieux, M. Contaldo, F. Giroud, D. Severac, M. Morgan, S. Gyger, C. Monneron, T.-C. Le, C. Henzelin, and V. Peiris, "A 1 V RF SoC with an 863-to-928 MHz 400 kb/s radio and a 32b dual-MAC DSP core for wireless sensor and body networks," in *Proc. IEEE Int. Solid-State Circuits Conf. (ISSCC)*, Feb. 2010, pp. 464–465.
- [6] M. Contaldo, B. Banerjee, D. Ruffieux, J. Chabloz, E. Le Roux, and C. C. Enz, "A 2.4-GHz BAW-based transceiver for wireless body area networks," *IEEE Trans. Biomed. Circuits Syst.*, vol. 4, no. 6, pp. 391–399, Dec. 2010.
- [7] J. Masuch and M. Delgado-Restituto, "A 190- μ W zero-IF GFSK demodulator with a 4-b phase-domain ADC," *IEEE J. Solid-State Circuits*, vol. 47, no. 11, pp. 2796–2806, Nov. 2012.
- [8] J. Masuch and M. Delgado-Restituto, "A 1.1-mW-RX -81.4-dBm sensitivity CMOS transceiver for bluetooth low energy," *IEEE Trans. Microw. Theory Tech.*, vol. 61, no. 4, pp. 1660–1673, Apr. 2013.
- [9] B. Banerjee, C. C. Enz, and E. Le Roux, "Detailed analysis of a phase ADC," in *Proc. IEEE Int. Symp. Circuits Syst. (ISCAS)*, May 2010, pp. 4273–4276.
- [10] Y. Liu, D. Zhao, Y. Li, and W. A. Serdijn, "A 5b 12.9 μ W charge-redistribution phase domain ADC for low power FSK/PSK demodulation," in *Proc. IEEE Eur. Solid State Circuits Conf. (ESSCIRC)*, Sep. 2014, pp. 275–278.
- [11] M. Pelgrom, *Analog-to-Digital Conversion*. Dordrecht, The Netherlands: Springer, 2010.
- [12] A. Papoulis and S. U. Pillai, *Probability, Random Variables, Stochastic Processes*, 4th ed. New Delhi, India: Tata McGraw-Hill, 2002.
- [13] W. Kester, *Data Conversion Handbook*. Oxford, U.K.: Elsevier, 2005.
- [14] G. Retz, H. Shanan, K. Mulvaney, S. O'Mahony, M. Chanca, P. Crowley, C. Billon, K. Khan, and P. Quinlan, "A highly integrated low-power 2.4 GHz transceiver using a direct-conversion diversity receiver in 0.18 μ m CMOS for IEEE802.15.4 WPAN," in *Proc. IEEE Int. Solid-State Circuits Conf. (ISSCC)*, Feb. 2009, pp. 414–415a.
- [15] Y.-H. Liu, X. Huang, M. Vidojkovic, A. Ba, P. Harpe, G. Dolmans, and H. de Groot, "A 1.9 nJ/b 2.4 GHz multistandard (Bluetooth Low Energy/Zigbee/IEEE802.15.6) transceiver for personal/body-area networks," in *Proc. IEEE Int. Solid-State Circuits Conf. (ISSCC)*, Feb. 2013, pp. 446–447.
- [16] A. Wong, M. Dawkins, G. Devita, N. Kasparidis, A. Katsiamis, O. King, F. Lauria, J. Schiff, and A. Burdett, "A 1 V 5 mA multi-mode IEEE 802.15.6/Bluetooth Low-Energy WBAN transceiver for biotelemetry applications," *IEEE J. Solid-State Circuits*, vol. 48, no. 1, pp. 186–198, Jan. 2013.
- [17] H.-Y. Tai, Y.-S. Hu, H.-W. Chen, and H.-S. Chen, "A 0.85 fJ/conversion-step 10b 200 kS/s subranging SAR ADC in 40 nm CMOS," in *Proc. IEEE Int. Solid-State Circuits Conf. (ISSCC)*, Feb. 2014, pp. 196–197.
- [18] B. Murmann, *Energy Limits in A/D Converters*, Aug. 2012 [Online]. Available: <http://ewh.ieee.org/r5/dallas/sscs/slides/20120829dallas.pdf>



biomedical applications.

Yao Liu was born in China, in 1987. He received the M.Sc. and B.Sc. degrees in electrical engineering from Huazhong University of Science and Technology, Wuhan, China, in 2008 and 2011, respectively. He is currently working towards the Ph.D. degree in the Bioelectronics Section of the Department of Microelectronics at the Faculty of Electrical Engineering, Mathematics, and Computer Science, Delft University of Technology, The Netherlands. His research interests include low power wireless communication circuits design for



Reza Lotfi (M'05–SM'14) received the B.Sc. degree from the Ferdowsi University of Mashhad, Mashhad, Iran, the M.Sc. degree from the Sharif University of Technology, Tehran, Iran, and the Ph.D. degree from the University of Tehran, Tehran, Iran, all in electrical engineering, in 1997, 1999, and 2004, respectively. Since 2004, he has been with the Ferdowsi University of Mashhad, where he is currently an Associate Professor. He has been with the Electronics Research Laboratory, Delft University of Technology, Delft, The Netherlands, from 2008 to 2009 as a Postdoctoral Scientific Researcher and then from February 2014 as a Visiting Professor. Dr. Lotfi has served as an Associate Editor for the IEEE TRANSACTIONS ON CIRCUITS AND SYSTEMS I: REGULAR PAPERS from 2010 to 2012. He has also served as the General Chair of 21st Iranian Conference on Electrical Engineering, ICEE 2013. His research interests include low-power analog and mixed-signal integrated circuit design.



Yongchang Hu (S'13) was born in Xi'an, China, in 1988. He received his B.Sc. and M.Sc. degrees from Northwestern Polytechnical University (NWPU), Xian, China, in 2010 and in 2013, respectively. He is currently pursuing his Ph.D. degree with the Circuits and Systems (CAS) Group, Department of Microelectronics, Delft University of Technology, The Netherlands. His research interests include signal processing for wireless communications, modelling radio propagation channel, random network analysis and wireless localization.



Wouter A. Serdijn (M'98–SM'08–F'11) was born in Zoetermeer ("Sweet Lake City"), The Netherlands, in 1966. He received the M.Sc. (cum laude) and Ph.D. degrees from Delft University of Technology, Delft, The Netherlands, in 1989 and 1994, respectively.

Currently, he is an Associate Professor at Delft University of Technology, where he heads the Bioelectronics Section. His research interests include low-voltage, ultra-low-power and ultra wide-band integrated circuits and systems for biosignal conditioning and detection, neuroprosthetics, transcutaneous wireless communication, power management and energy harvesting as applied in, e.g., hearing instruments, cardiac pacemakers, cochlear implants, neurostimulators, portable, wearable, implantable and injectable medical devices, and electroceuticals. He is co-editor and co-author of the books *EML-Resilient Amplifier Circuits* (Springer 2013), *Ultra Low-Power Biomedical Signal Processing: An Analog Wavelet Filter Approach for Pacemakers* (Springer, 2009), *Circuits and Systems for Future Generations of Wireless Communications* (Springer, 2009), *Power Aware Architecting for Data Dominated Applications* (Springer, 2007), *Adaptive Low-Power Circuits for Wireless Communications* (Springer, 2006), *Research Perspectives on Dynamic Translinear and Log-Domain Circuits* (Kluwer, 2000), *Dynamic Translinear and Log-Domain Circuits* (Kluwer, 1998), and *Low-Voltage Low-Power Analog Integrated Circuits* (Kluwer, 1995). He authored and co-authored 8 book chapters and more than 250 scientific publications and presentations. He teaches circuit theory, analog signal processing, micropower analog IC design, and bioelectronics.

Prof. Serdijn received the Electrical Engineering Best Teacher Award in 2001 and 2004. He has served, a.o., as General Chair for IEEE BioCAS 2013, Technical Program Chair for IEEE BioCAS 2010 and as Technical Program Chair for IEEE ISCAS 2010, 2012 and 2014, as a member of the Board of Governors (BoG) of the IEEE Circuits and Systems Society (2006–2011), as chair of the Analog Signal Processing Technical Committee of the IEEE Circuits and Systems society, as a member of the Steering Committee of the IEEE Transactions on Biomedical Circuits and Systems (T-BioCAS) and as Editor-in-Chief for IEEE TRANSACTIONS ON CIRCUITS AND SYSTEMS—I: REGULAR PAPERS (2010–2011). He currently is General Co-Chair for IEEE ISCAS 2015. He is an IEEE Distinguished Lecturer and a mentor of the IEEE.